applied sciences

MDPI

Article

Effects of CO_2 Concentration During Curing on Carbon Sequestration and Strength of Coal-Based Solid Waste Backfill

Wenchang Feng [1], Daoxiong Zhang [1], Meng Li [1,*], Binbin Huo [1], Yuyin Guo [2], Yazhou Shi [2], Zhangyu Li [1] and Yunkai Zhang [1]

[1] State Key Laboratory for Fine Exploration and Intelligent Development of Coal Resources, School of Mines, China University of Mining and Technology, Xuzhou 221116, China; fengwenchang@cumt.edu.cn (W.F.); 18759399368@163.com (D.Z.); huobinbin@cumt.edu.cn (B.H.); ts25020158p31@cumt.edu.cn (Z.L.); ts25020070a31@cumt.edu.cn (Y.Z.)

[2] Jining Jinqiao Coal Mine, Jining 272200, China; jadeseal@126.com (Y.G.); asiaook@126.com (Y.S.)

* Correspondence: limeng1989@cumt.edu.cn

Abstract

Coal development produces large amounts of coal-based solid wastes (coal gangue, slag, fly ash) and substantial CO_2 emissions, posing severe ecological burdens on mining areas. This study integrated coal-based solid-waste cemented backfilling with CO_2 mineral sequestration to co-dispose of coal-based solid wastes and CO_2, experimentally investigating the CO_2 sequestration performance and uniaxial compressive strength (UCS) of coal-based solid-waste cemented backfill (CSCB) under mineralization curing with different CO_2 concentrations. TG-DTG, SEM-EDS, and XRD were adopted to investigate the CO_2 mineral sequestration process and the strength reduction of CSCB. The TG-DTG-based calculated CO_2 uptake of CSCB was positively correlated with the CO_2 concentration, rising by 86.9% from 2.52% to 4.71% as the concentration increased from 1.5% to 10%. In contrast, CSCB UCS decreased drastically by 88.1% from 6.05 MPa to 0.72 MPa when concentration increased from 0 to 10%. The combined microcharacterization results suggest that CO_2 reacted with alkaline substances and hydration products (CH, C-(A)-S-H gel, AFt) in CSCB to form carbonates. The UCS reduction is interpreted as arising mainly from a weakened alkaline environment (according to results and speculation), degradation of the C-(A)-S-H gel, and the AFt–CO_2 substitution reaction. Within the investigated conditions (a single mix proportion and a 14-day curing age), this study provides a reference for coal-based solid-waste backfilling coupled with CO_2 mineral sequestration; extrapolation to other mix proportions, longer curing ages, or field-scale applications requires further verification.

Keywords: coal-based solid waste; CO_2 sequestration; backfill material; waste valorization; mechanical performance

Check for updates

Academic Editors: Dibyendu Sarkar and Antonio Bernardo Sánchez

Received: 14 July 2026
Revised: 5 September 2026
Accepted: 14 September 2026
Published: 15 September 2026

Copyright: © 2026 by the authors. Licensee MDPI, Basel, Switzerland. This article is an open access article distributed under the terms and conditions of the Creative Commons Attribution (CC BY) license.

1. Introduction

With the acceleration of global industrialization, the CO_2 concentration increases constantly, which has become a core issue among those seeking to ameliorate the effects of global climate change [1,2]. In the CO_2 Emissions in 2024 issued by the International Energy Agency in 2025, the total CO_2 emissions related to the energy in 2024 increased by 0.8%, reaching a record high of 37.8 billion tons of CO_2 emissions. Due to such an increase, the atmospheric CO_2 concentration in 2024 reached 422.5 ppm, which was 3 ppm higher than that in 2023 and 50% higher than pre-industrial levels. Over 100 major economies, including the UK, China, and the US, have established net-zero greenhouse gas emission

targets through laws, policy documents, or government statements [3–6]. For example, in September 2020, the Chinese Government solemnly announced the target of reaching the goals of carbon peaking by 2030 and carbon neutrality by 2060 [7], highlighting the steadfast determination of the nation in cutting greenhouse gas emissions [8,9]. To reach these goals, various sectors should take positive measures to reduce CO_2 emissions, which is not only of important significance for efforts in carbon emission reduction but also a key link to slow down climate change [10].

The large amounts of coal-based solid wastes including coal gangue (CG), fly ash (FA), and slag associated with the mining and utilization of coal show a low resource utilization level and a lack of large-scale consumption channels. Their ground storage or landfilling also may cause severe environmental pollution [11,12]. The coal-based solid-waste cemented backfilling technique can make full use of the goaf in coal mines to achieve large-scale disposal of coal-based solid wastes and effectively addresses the aforementioned problem. It follows this principle: coal-based solid wastes such as CG, FA, and slag are used to prepare cemented slurry and then backfilled in the goaf, forming a stable load-bearing body to control ground pressure and surface deformation [13,14]. In addition, CO_2 mineral sequestration, as a key technique used to reduce carbon emissions, can sequestrate CO_2 by simulating the natural process, in which CO_2 reacts with calcium (Ca) and magnesium (Mg) minerals to produce carbonates [15–18]. The key point for combination of the two is that the coal-based solid-waste filling body is rich in CaO and MgO needed for reactions and its porous structure significantly promotes the CO_2 mineralization reaction and sequestration [19–21]. Therefore, if the coal-based solid-waste cemented backfilling can be combined with CO_2 mineral sequestration, the dual goals of resource utilization of coal-based solid wastes and CO_2 mineral sequestration are achieved.

Regarding the CO_2 mineral sequestration methods and techniques using solid wastes, various studies have revealed the correlations among different influencing factors and material performance. As for material optimization, some researchers improved the mineralization potential of solid wastes through modification. For example, Cheng et al. [22] proposed to enhance CO_2 mineralization via amine-looping, by which the CO_2 sequestration capacity of steel slag increases from 114.4 g/kg to 202.4 g/kg (an increase of 77%) and that of iron tailings grows from 12.6 g/kg to 50.6 g/kg (an increase of 302%). Sun et al. [23] prepared a backfill material with a certain CO_2 sequestration capacity using Mg-slag slurry formed through compound modification of physicochemical methods. Guo et al. [24] found via orthogonal experiments that the total sequestered CO_2 of gangue-based mineralized backfill materials exhibits a positive correlation with the water–cement ratio. After 45 min of stirring and carbonation, the backfill materials achieved a maximum total sequestered CO_2 of 18.96 g/kg, with a maximum CO_2 sequestration rate of 0.20 $g \cdot kg^{-1} \cdot min^{-1}$. By adding biochar modified by acid, alkali, and amine in the solid waste-based lightweight aggregate, Yan et al. [25] constructed a composite system and optimized the pore structure and reaction activity. Consequently, the rate of mineralization increased by 50% and synergy in the resource utilization of solid wastes and carbon-negative emissions was achieved. The regulatory effect of environmental parameters on the mineralization process has also attracted much attention. Pan et al. [26] significantly enhanced the CO_2 mineralization reaction and amount of CO_2 sequestrated by steel slag through optimizing the temperature parameters; they eventually prepared a high-performance mineralized building material. He et al. [27] used multiple indices to characterize the basic properties of the backfill of reservoirs after two years of carbonization. They found that the long-term hydration positively affects the performance of the concrete and revealed the adverse effects of two years of carbonization on the performance of the backfill material. Noh et al. [28] achieved CO_2 sequestration while recovering manganese (Mn) by using blast furnace slag, electric arc

furnace slag, and their dust through the pH swing-assisted carbonization process. Moreover, microbial-induced mineralization, as an emerging technology, also shows its potential. Wilcox et al. [29] compared the merits of the microbial-induced carbonate precipitation and the carbonation of chemical minerals in terms of CO_2 sequestration. They found that the energy demand of the former is 60% lower and the CO_2 sequestration efficiency is 30% higher than the latter, providing a new idea for CO_2 capture and sequestration. Li et al. [30] studied a promising method of utilization of steel slag to microbial-induced carbonation of minerals, and analyzed the strengthening principle and factors influencing carbonation of steel slag. Previous researchers have garnered fruitful achievements in the modification of solid wastes, optimization of environmental parameters, and microbial-induced mineralization. However, the CO_2 mineral sequestration mechanisms of non-modified multi-source coal-based solid-waste cemented backfill (CSCB) materials are seldom studied. In addition, the effects of CO_2 mineral sequestration on the mechanical performance of coal-based solid wastes and the microscopic mechanisms remain unclear.

In view of this, the CO_2 mineral sequestration effect and the mechanical performance of CSCB cured at different CO_2 concentrations were experimentally investigated. The evolution of the CO_2 uptake and uniaxial compressive strength (UCS) of CSCB cured at different CO_2 concentrations were analyzed through thermogravimetric (TG) analysis and uniaxial compression tests. Modern analysis approaches such as scanning electron microscopy-energy dispersive x-ray spectroscopy (SEM-EDS) and X-ray diffraction (XRD) were employed to investigate and interpret the mechanisms underlying the CO_2 mineral sequestration and the strength reduction of CSCB on the basis of the combined experimental evidence. To this end, the research aims to provide a reference for understanding coal-based solid-waste backfilling coupled with CO_2 mineral sequestration under the investigated laboratory conditions.

2. Materials and Methods

2.1. Raw Materials

CSCB used in the experiment was prepared by three coal-based solid wastes including CG, FA, and coal-fired power plant bottom ash (BA) collected from the CG storage bin and power plant of a coal mine in Shandong Province, China, as well as PO42.5 Portland cement (PC), purchased from Anhui Conch Cement Co., Ltd., Wuhu, China. The phase compositions of the raw materials were analyzed through XRD, and the oxide compositions and contents were measured via X-ray fluorescence (XRF) analysis, with measured results shown in Figure 1 and Table 1. The composition of CG included quartz and kaolinite, in which SiO_2 and Al_2O_3 accounted for large proportions of the total by mass; FA mainly contained quartz, mullite, and calcite, in which the total proportion of SiO_2 and Al_2O_3 exceeded 50% and the proportion of CaO was as high as 15.08%. The main minerals in BA included quartz, calcite, and anhydrite, in which the total proportion of SiO_2 (49.27%) and Al_2O_3 (28.82%) was approximated to 80%. Cement served as the core cementitious material, the main minerals in which were quartz, calcite, alite (C_3S, Ca_3SiO_5), belite (C_2S, Ca_2SiO_4), and gypsum, in which CaO accounted for 51.30%. Given that the MgO content in the above materials is negligible, it will not be emphasized in the subsequent mechanistic analysis.

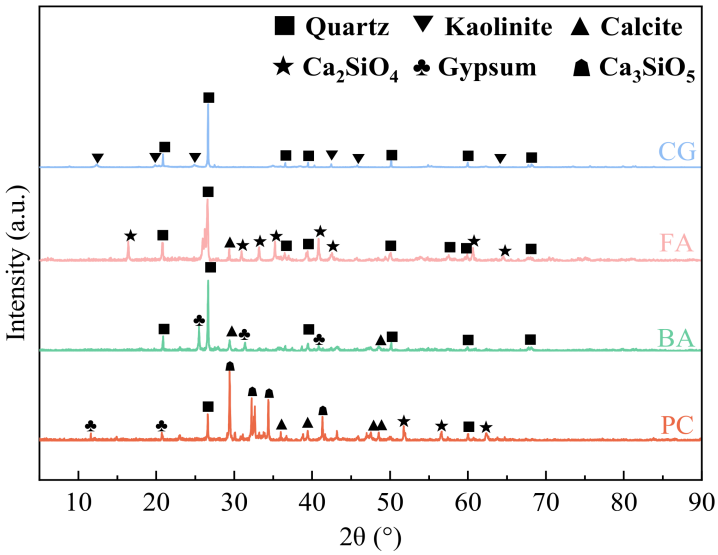


Figure 1. XRD patterns of the experimental materials.

Table 1. Main oxide compositions and contents of the experimental materials.

wt%	SiO_2	Al_2O_3	CaO	MgO	Fe_2O_3	K_2O	TiO_2	SO_3	Others
CG	52.21	22.27	0.56	0.56	2.71	2.28	0.93	0.98	17.50
FA	35.11	22.66	15.08	0.94	5.53	1.32	1.07	4.73	13.56
BA	49.27	28.82	8.32	0.58	6.67	1.62	2.38	0.94	1.40
PC	25.98	11.33	51.30	0.64	5.05	1.33	0.69	2.34	1.34

2.2. Sample Preparation and Test System

2.2.1. CO_2 Sequestration System

As illustrated in Figure 2, the CO_2 sequestration test system of CSCB consisted of two parts: a curing and mineralization system and a gas-supply system. The core component of the curing and mineralization system was a mineralization box of the backfill material. Sensors for temperature, humidity, and gas detection were installed in the mineralization box, along with a heat dissipation and dehumidification device. By setting the target temperature, humidity, and CO_2 concentration using the numerical control panel on the box, the system could automatically adjust the ambient parameters of mineralization in the box within these ranges: the humidity, temperature, and CO_2 concentration were separately controlled within ranges of 0 to 99.9%, room temperature to 100 °C, and 0 to 100%, respectively. During the tests, sensors continuously monitor the CO_2 concentration inside the chamber and feed the signals back to the controller in real time. When the measured concentration drops below the setpoint, the controller automatically opens the solenoid valve to supply CO_2 into the chamber, while simultaneously activating the internal fan to ensure gas uniformity. Once the concentration returns to the setpoint, the solenoid valve is closed. Through this mechanism, the CO_2 concentration in the chamber is stably controlled within ±3% of the target value. Meanwhile, the temperature and relative humidity inside the chamber are independently maintained within ±2 °C and ±5% of their respective target values via separate sensors and controllers. Throughout the entire testing period, all parameters are automatically recorded by the system. An insulation and explosion-proof box and a CO_2 container were the main components of the gas-supply system, which was linked to the curing and mineralization system. Therein, a single gas container had a volume of 40 L, which was filled with liquid CO_2 (purity 99.999%) and could meet the gas requirement in the test process.

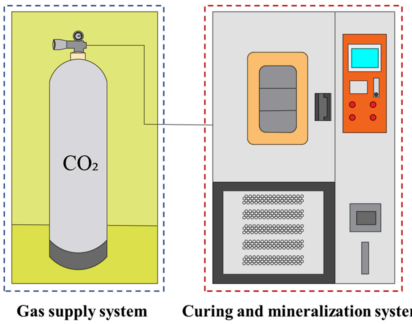


Figure 2. The CO_2 sequestration test system.

2.2.2. Sample Preparation

The preparation process of experimental materials included three stages: preprocessing of raw materials, sample preparation, and demolding and curing. At first, after breaking the CG using a jaw crusher (Lichen Scientific Instrument Co., Ltd., Shaoxing, China), the CG particles were subjected to graded screening using square-aperture sieves with aperture sizes of 1, 2.5, and 5 mm to obtain particles finer than 5 mm. Meanwhile, BA particles finer than 1 mm were screened. After drying all raw materials, namely, CG, FA, BA, and cement in a drying box at 105 °C for 24 h, these materials were sealed and preserved for later use. During sample preparation, after weighing each component, using an electronic scale (Delixi Electric Co., Ltd., Wenzhou, China) with the precision of 0.01 g according to the designed proportion ratios, and adding tap water in the laboratory, these materials were mixed in a blender for 3 to 5 min to form the uniform slurry. The slurry was poured into molds measuring 70.7 mm × 70.7 mm × 70.7 mm and the surface was covered by a film to prevent water loss. After standing for 24 h, the samples were demolded and transferred to the mineralization curing box to be cured for the specified curing period (14 d) under a relative humidity of 65% at 25 °C.

2.3. Test Schemes

To assess the CO_2 sequestration effect of CSCB and its mechanical performance under CO_2 mineral sequestration, the one-factor-at-a-time method was adopted to design test schemes to investigate the influences of the CO_2 concentration on the performance of CSCB.

In the curing and maintenance stage, CO_2 molecules constantly diffused and entered the interior of the filling body. Within a fixed space, the CO_2 concentration directly determines the number of CO_2 molecules in the space. On this basis, test schemes for the performance of CSCB under the influences of the CO_2 concentration were designed, as listed in Table 2. The solid content refers to the mass proportion of solids in the filling material. The mineralization period was designed to be 14 d. The curing conditions are humidity of 65 ± 5% and temperature of 25 °C. The 14-day curing age was selected to isolate the short-term effect of the CO_2 concentration at a constant sample age, and it does not represent a long-term performance assessment.

Table 2. Test schemes for CSCB performance under CO_2 concentration.

No.	G0	G1.5	G2.5	G5.0	G7.5	G10
CO_2 volume concentration (%)	0	1.5	2.5	5	7.5	10
Solid content (%)	68					
Fly ash content (wt%)	40					
Slag content (wt%)	30					
Coal gangue (wt%)	18					
Cement content (wt%)	12					

2.4. Test Methods

2.4.1. CO_2 Sequestration Performance Tests

A THG-205 thermogravimetric analyzer (Nanjing Dazhan Testing Instrument Co., Ltd., Nanjing, China) was used to measure the CO_2 uptake of CSCB. The five-point sampling method was employed to collect powder of the CSCB samples. The sample powder (8–10 mg) was placed in a small built-in crucible, which was placed on a balance integral to the device with tweezers, to which high-purity N_2 was injected after stabilization of dial readings. The temperature was set to 25 °C and the temperature was increased at 20 °C/min (to a potential maximum of 1000 °C). The TG and derivative thermogravimetric (DTG) curves were obtained using the device. The five-point sampling covered the specimen volume, and the homogenized powder was prepared by thoroughly mixing material collected from these positions; it therefore reflects the bulk-average carbonation state of the specimen rather than only a surface layer.

After determining the decomposition and weight loss zones of carbonates according to the TG-DTG curves, the CO_2 uptake of CSCB was calculated thus:

$$\text{CO}_2 \text{ uptake} = \left(\frac{\omega_i - \omega_j}{\omega_j} - \frac{\omega_{i\text{-NCO}_2} - \omega_{j\text{-NCO}_2}}{\omega_{j\text{-NCO}_2}} \right) \cdot 100\% \quad (1)$$

where CO_2 uptake is the actual CO_2 uptake of CSCB (%); ω_i and ω_j are the percentages of residual masses of samples after mineral sequestration at i °C and j °C on TG curves in the mass of mineralized samples ($i < j$) (%); $\omega_{i\text{-NCO}_2}$ and $\omega_{j\text{-NCO}_2}$ represent the percentages of residual masses of unmineralized samples at i °C and j °C on TG curves in the mass of original samples without the reaction ($i < j$) (%).

2.4.2. Mechanical Tests

After mineralizing and curing the samples for 14 d, the mechanical performance of CSCB before and after mineralization was analyzed by measuring the compressive strength. All specimen end faces were ground flat prior to compressive strength testing. The specimens were fixed on a surface grinding machine. They were first rough-ground and then fine-ground. After the machining process, the flatness of the end faces was checked using a straightedge and a feeler gauge to ensure that both end faces were flat and parallel to each other. The out of parallelism of the end faces was controlled to be less than 0.05 mm, and the deviation of perpendicularity between the end face and the longitudinal axis was maintained within 0.25°. Each face of the sample was ground flat, and then the sample was tested using a WAW-1000D universal hydraulic servo-motor controlled testing machine (Changchun Sinter Testing Machine Co., Ltd., Changchun, China) at a constant-displacement loading rate of 0.5 mm/min. The peak stress and displacement in the loading process to failure were recorded. Three samples were tested in each group, and their arithmetic mean value was calculated to ensure the reliability of tests.

2.4.3. Microstructures and Chemical Components Tests

A Zeiss Sigma360 SEM (Carl Zeiss AG, Oberkochen, Germany) was adopted to observe the microstructures of samples before and after mineralization. The energy dispersive spectroscopy (EDS) spectrometer equipped could analyze the contents of main elements at different test points. Blocks within 10 mm of the center of the samples were taken (a flat surface opposite the natural fracture was retained), of which the hydration reaction was terminated by soaking in absolute ethyl alcohol for 12 h and drying at 50 °C for 24 h. The sample was fixed to the base using conductive tape (Nisshin EM Co., Ltd., Tokyo, Japan). After metal spray-coating of the test surface, the micro-morphology was photographed

under 5000× magnification. Furthermore, the EDS was used to select and analyze points on the test surface, to obtain the elemental composition at each point.

A Smart Lab SE X-ray diffractometer (Rigaku Corporation, Tokyo, Japan) was used for X-ray diffraction measurements of both raw materials and mineralized CSCB samples to characterize mineral-component variations. The samples were ground to powder and screened via a sieve of 200 mesh. The scanning range and scanning rate were set to 5 to 90° and 5°/min, respectively. This scanning configuration is intended for qualitative phase screening; quantitative phase abundances were not determined. Phase identification of XRD patterns was performed using Jade 6.5 software (Materials Data Inc., Livermore, CA, USA).

Oxide compositions of raw materials were obtained by X-ray fluorescence (XRF) analysis using a ZSX Primus spectrometer (Rigaku Corporation, Tokyo, Japan).The CO_2 sequestration effect and mechanical performance of CSCB were studied based on the aforementioned test schemes and methods. The specific test flowchart is shown in Figure 3.

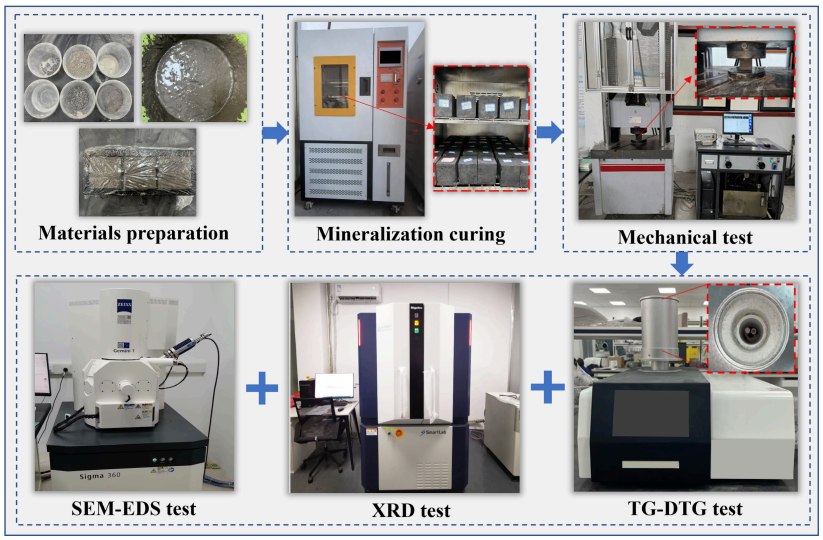


Figure 3. Test flowchart for CO_2 sequestration effect and CSCB mechanical performance.

3. Results and Discussion

3.1. CO_2 Sequestration Performance

For qualitative analysis of thermal decomposition stages and weight-loss characteristic intervals, four representative groups (G0, G1.5, G5, G10) were selected to plot the TG-DTG profiles, as displayed in Figure 4, which can sufficiently reflect the overall thermal reaction law of the backfill specimens.

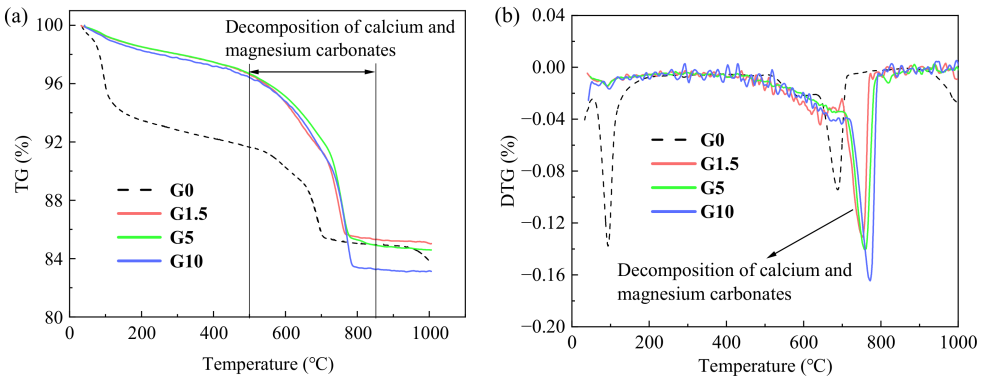


Figure 4. TG (**a**) and DTG (**b**) curves of CSCB under curing with different CO_2 concentrations.

According to analysis of Figure 4, the TG curves of carbonation-cured samples (G1.5, G5, G10) are divided into three stages: slow weight loss (25 to 500 °C), rapid weight loss (500 to 850 °C), and stabilization (850 to 1000 °C) stages. The first stage is mainly a result of joint action of the adsorbed water, bound water, and decomposition of hydration products; in the second stage, significant weight loss peaks appear on the DTG curves, corresponding to the decomposition of carbonates; the TG curves become stable in the third stage, suggesting that the decomposition of carbonates of low crystallinity is practically complete. It should be noted that the MgO mass fraction of all raw materials is less than 1 wt% (Table 1). Accordingly, the carbonate decomposition interval adopted in this study mainly refers to the decomposition range of calcium carbonate. All subsequent calculations are conducted on this premise, and mass losses originating from magnesium carbonate and other carbonate phases are neglected.

A prominent distinction among the DTG curves is the intense mass-loss peak at approximately 100 °C for the non-carbonated reference (G0), which is almost completely absent in all carbonated specimens (G1.5, G5, and G10). The intense mass-loss peak at approximately 100 °C for G0 may be associated with the release of interlayer water retained within the C-S-H gel structure. The near absence of this peak in the carbonated specimens could possibly reflect the decalcification and disruption of the C-S-H layered framework upon CO_2 attack. Meanwhile, the carbonation-induced micro-cracking, which is likely linked to the observed reduction in compressive strength, might have facilitated the escape of free water during sample preparation. This tentative interpretation appears to be broadly consistent with the concurrent changes in the mid- and high-temperature regions, where the CH peak gradually diminishes while the carbonate decomposition peak becomes more pronounced with increasing CO_2 concentration. At 500–850 °C, in the uncarbonated reference G0, the mass-loss event near ~700 °C is attributed to the decomposition of pre-existing carbonates in the raw materials (e.g., calcite in FA and BA and trace limestone filler in the cement), the weight loss peak of mineralized samples shifts rightwards, indicative of the increase in the content of carbonate minerals and the improvement of the crystallinity. Therefore, calculation of CO_2 uptake should be benchmarked by changes in the weight loss on TG curves in the range of 500 to 850 °C, and the original carbonate content in the raw materials should be deducted, as expressed in Equation (2).

$$\text{CO}_2\text{ uptake} = \left(\frac{\omega_{500\ ^\circ\text{C}} - \omega_{850\ ^\circ\text{C}}}{\omega_{850\ ^\circ\text{C}}} - \frac{\omega_{500\ ^\circ\text{C-NCO}_2} - \omega_{850\ ^\circ\text{C-NCO}_2}}{\omega_{850\ ^\circ\text{C-NCO}_2}} \right) \cdot 100\% \quad (2)$$

where CO_2 uptake is the actual CO_2 uptake of CSCB (%); $\omega_{500\ ^\circ\text{C}}$ and $\omega_{850\ ^\circ\text{C}}$ represent the percentages of residual masses of mineralized samples at 500 °C and 850 °C on TG curves in the mass of mineralized samples (%); $\omega_{500\ ^\circ\text{C-NCO}_2}$ and $\omega_{850\ ^\circ\text{C-NCO}_2}$ stand for the percentages of residual masses of unmineralized samples at 500 °C and 850 °C on TG curves in the mass of raw unmineralized samples (%), respectively.

Influences of the CO_2 concentration on the CO_2 uptake of CSCB are shown in Figure 5 and Table 3.

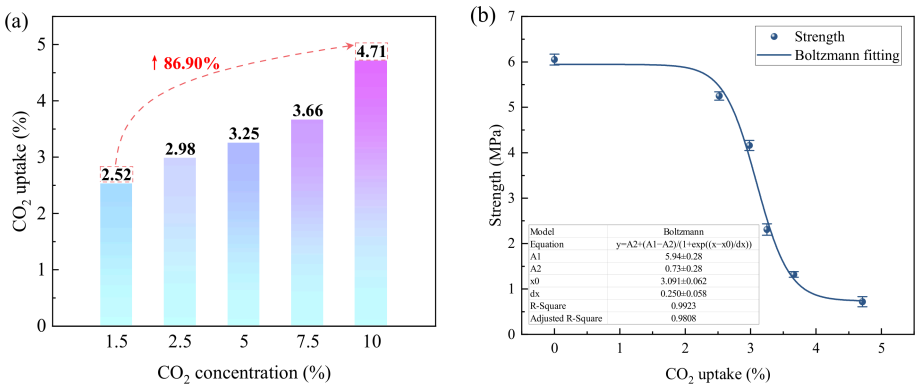


Figure 5. CO_2 uptake of CSCB under curing with different CO_2 concentrations (**a**) and fitting curve of CSCB strength versus CO_2 uptake (**b**).

Table 3. Calculated CO_2 uptake under the influences of different CO_2 concentrations.

No.	$\omega_{500\,^\circ C}$ (wt%)	$\omega_{850\,^\circ C}$ (wt%)	$\omega_{500\,^\circ C\text{-}NCO_2}$ (wt%)	$\omega_{850\,^\circ C\text{-}NCO_2}$ (wt%)	CO_2 Uptake (wt%)
G1.5	96.786	87.423			2.52
G2.5	96.569	86.869			2.98
G5	96.411	86.516	91.671	84.731	3.25
G7.5	95.426	85.314			3.66
G10	96.221	85.226			4.71

Analysis of Figure 5 shows that:

As the CO_2 concentration in the curing environment rises, the CO_2 uptake of CSCB increases significantly. As the CO_2 concentration increases from 1.5% to 10%, the CO_2 uptake increases by 86.90% from 2.52% to 4.71%. As the CO_2 concentration increases, the number of CO_2 molecules in the curing space increases significantly, with enhanced permeability to the interior of the material. Consequently, the contact probability and reaction frequency of CO_2 molecules with active minerals in the filling body are significantly improved, driving a substantial increase in the CO_2 uptake.

The Boltzmann model was used in the non-linear regression analysis of the relationship between the strength and CO_2 uptake of CSCB. The results are illustrated in Figure 5b. The coefficient of determination R^2 and adjusted R^2 values of the fitting curves are 0.9923 and 0.9808, respectively. Given that the fit is based on only five mineralized CO_2 concentrations, these values describe the closeness of the fit to the observed data rather than demonstrating high predictive reliability. However, due to the limited number of experimental data points, the asymptotes of the fitted curve are only for reference and accompanied by considerable uncertainty. The fitting results mainly reflect the overall variation trend of the data. Although no parallel TG-DTG tests or independent validation by an alternative technique were performed for the calculated CO_2 uptake, the monotonic increase in the calculated uptake with the CO_2 concentration is consistent with the strong inverse correlation between UCS and the CO_2 concentration and with the high repeatability of the parallel UCS tests (Figure 6).

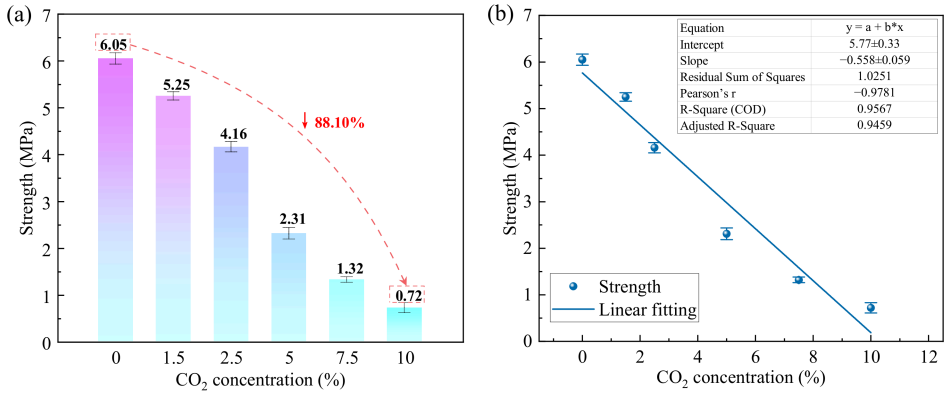


Figure 6. UCS of CSCB under different CO_2 concentrations (**a**) and its fitting curve (**b**). Error bars represent the standard deviation (SD) of three parallel experiments (n = 3).

3.2. Mechanical Performance

Changes in the compressive strength of CSCB under the influences of the CO_2 concentration are illustrated in Figure 6. To ensure the reliability of strength data through parallel tests, three uniaxial compressive strength (UCS) tests were conducted for each group, with the average value calculated and the standard deviation (SD) determined.

Triplicate specimens were prepared for each test condition (n = 3). The maximum SD of uniaxial compressive strength (UCS) values was 0.125, which demonstrates excellent test repeatability and reliable experimental data. One-way analysis of variance further indicated that the p-value of UCS measurements from parallel samples cured under identical CO_2 concentrations was less than 0.05.

The UCS of CSCB declines significantly with rising CO_2 concentration. At CO_2 concentrations of 1.5% and 2.5%, the UCS of CSCB is 5.25 MPa and 4.16 MPa, respectively. Compared with the non-carbonated cured specimens (6.05 MPa), the strength decreases by 13.22% and 31.24%. When the CO_2 concentration rises to 5%, the UCS drops to 2.31 MPa, and the strength reduction sharply increases to 61.82%. This interval shows the largest increment in strength loss. When the CO_2 concentration further increases to 10%, the UCS falls below 1 MPa (0.72 MPa), with a strength reduction of 88.10%.

Engineering requirements for the strength of backfilling materials vary greatly. Based on existing research and engineering practices, backfilling materials intended mainly for solid-waste disposal have relatively low strength demands. Their early-age strength is generally required to reach 0.15–0.3 MPa. By contrast, backfilling applied to support overlying roof strata may require strength higher than 4 MPa [31]. In view of the above findings, CSCB prepared under 10% CO_2 concentration (0.72 MPa) can still meet the application requirements if supporting overlying roof strata is not needed. For cases with high requirements for supporting overlying roof strata, the CO_2 concentration should not exceed 2.5%.

The relationship between the UCS of CSCB and the CO_2 concentration was linearly fitted, with results shown in Figure 6b. The Pearson's r value is −0.9781, of which the absolute value is approximated to 1, suggesting when the CO_2 concentration ranges from 0% to 10%, there exists an extremely close negative linear relationship between the UCS of CSCB and the CO_2 concentration in this experiment. That is, the UCS declines significantly with the rise of the CO_2 concentration. The R^2 is 0.9567 and the adjusted R^2 is 0.9459, both greater than 0.9, meaning that the model can explain more than 95% of variation of the dependent variable (UCS) and has good fitting accuracy. The slope and intercept of the fitting results both vary within small ranges, and the residual sum of squares is 1.0251, suggesting that the model describes the observed negative linear influence of the CO_2

concentration on the UCS within the tested range; its predictive capability beyond the investigated conditions has not been established.

3.3. Components and Microstructures

3.3.1. EDS Analysis of Elements in the Products

Considering the cost and sample-preparation difficulty of SEM-EDS mapping analysis, the fracture plane in the middle of the samples after curing and mineralization for 14 d at a 5% CO_2 concentration (G5) was selected for map scanning. The selection rationale is as follows: As shown in Figure 6, when the CO_2 concentration exceeded 5%, the UCS of the cemented paste backfill exhibited a significant turning-point decline (a reduction of 42.9%), indicating that this concentration represents the critical threshold at which carbonation reaction shifts from "strength fine-tuning" to "structural deterioration". Furthermore, specimens at higher concentrations (G7.5 and G10) suffered from excessive carbonation, resulting in a loose structure that made it difficult to prepare flat polished cross sections meeting the requirements for quantitative EDS analysis. Therefore, the EDS results from G5 can most effectively reveal the typical microscopic mechanism during the transition from the early stage to the progressive development stage of carbonation. The elemental distribution obtained by scanning the micro-morphologies under a 5000× magnification is shown in Figure 7.

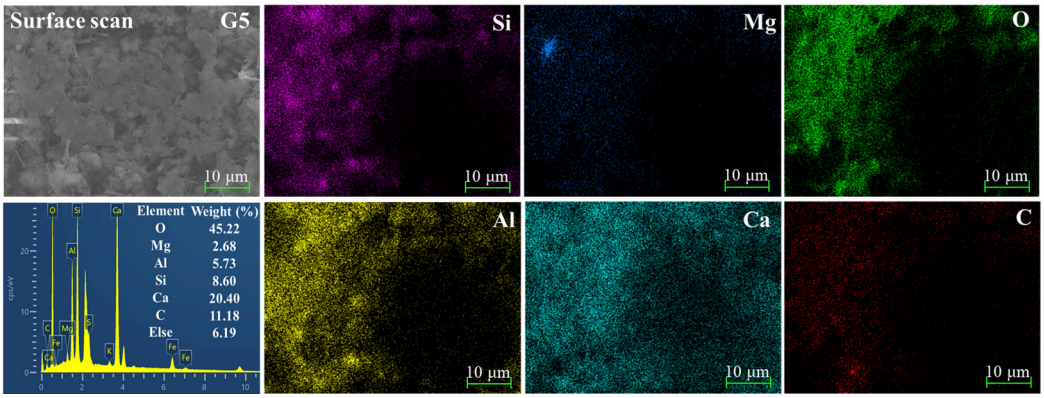


Figure 7. EDS characteristics of products after CSCB curing and mineralization.

Analysis of Figure 7 shows that:

The main elements in the samples include O (45.22%), Ca (20.40%), C (11.18%), Si (8.60%), and Al (5.73%), along with a relatively low content of Mg (2.68%), suggesting that Mg participates in the reaction at only trace concentrations.

Si, Al, and O are concentrated in local areas in the samples, suggesting that the gel content in the samples is relatively low and the hydration reaction is inhibited; most Si and Al are properly present as silicates or hydrated aluminosilicate compounds. These compounds may come from the raw materials or be formed due to the decomposition of hydration products such as gels by mineralization.

In terms of distribution of atomic weights, Ca and C are abundant and significant superpositions on the distribution patterns, indicating the presence of large amounts of carbonate minerals such as calcium carbonate and the high frequency of occurrence of mineralization reactions.

3.3.2. Evolution of Microstructures

The microstructures in the CSCB samples under the influences of the CO_2 concentration in the curing and mineralization stage are shown in Figure 8.

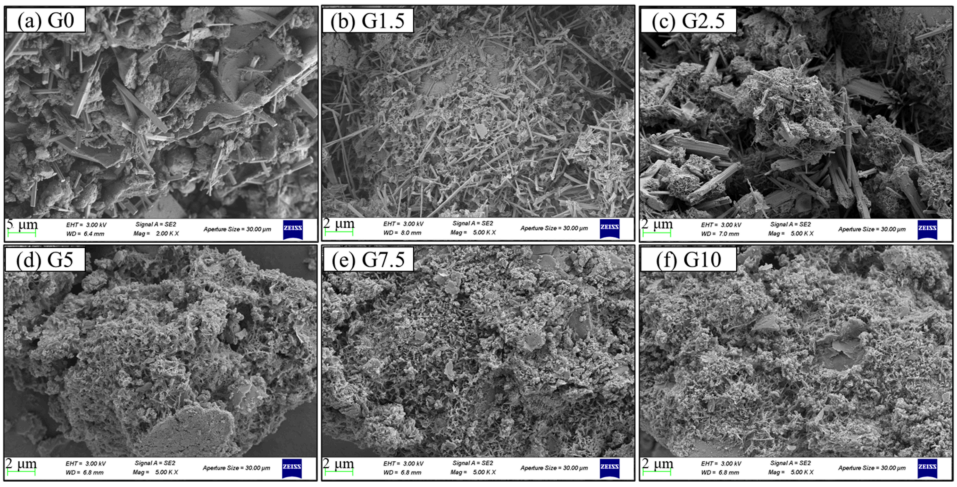


Figure 8. SEM micro-morphologies of CSCB under curing with different CO_2 concentrations.

According to analysis of Figure 8:

With increasing CO_2 concentration, the secondary products progressively cover the surfaces of the particle agglomerates, while the integrity of the internal pores and the skeletal framework declines and the honeycomb-like structures and particle agglomerates become looser. Flaky/laminar, massive, acicular, and rod-like morphological features appear within the gaps between particles and inside the honeycomb structures. From these morphological observations alone, it can only be reasonably inferred that carbonation/mineralization takes place preferentially in the vicinity of the hydration products (gels and particle agglomerates), consuming the active mineral components there. The exact identity of the newly formed or consumed phases cannot be established from microstructure alone and is instead determined by the XRD, EDS, and TG–DTG evidence presented in Sections 3.1, 3.3.1 and 3.3.3.

As the CO_2 concentration rises, increasing amounts of massive and laminar features gradually cover the particle-agglomerate surfaces and the pore walls. These morphological changes are consistent with the precipitation of carbonation products, which is independently confirmed by the Ca–C co-enrichment revealed in the EDS mapping (Section 3.3.1) and by the systematic growth of the calcite reflection in the XRD patterns (Section 3.3.3). At 7.5% and 10% CO_2, the honeycomb-like structures are further loosened and reduced in amount, suggesting that the original gel/skeleton may be decomposed or displaced under high-concentration carbonation. The assignment of these features to specific minerals is, however, deferred to the XRD, EDS, and TG–DTG results rather than claimed from SEM morphology.

Although the particle surfaces after high-concentration CO_2 curing appear to be coated by more secondary products, more voids and cracks are also observed between the particles. This increasingly loose and cracked microstructure is reasonably regarded as an important microstructural cause of the decrease in compressive strength reported in Section 3.2.

3.3.3. Changes in the Mineral Components

Changes in the mineral components of CSCB at different CO_2 concentrations in the curing and mineralization stage are shown in Figure 9. Phase identification was performed qualitatively by matching the observed reflections with standard ICDD Powder Diffraction File (PDF) cards; no Rietveld quantitative refinement was attempted, so the assignments are indicative and the intensities are treated comparatively rather than absolutely. The characteristic reflections adopted for each phase and their PDF card numbers are provided in the preceding analysis (Section 3.3.3) and in the legend of Figure 9.

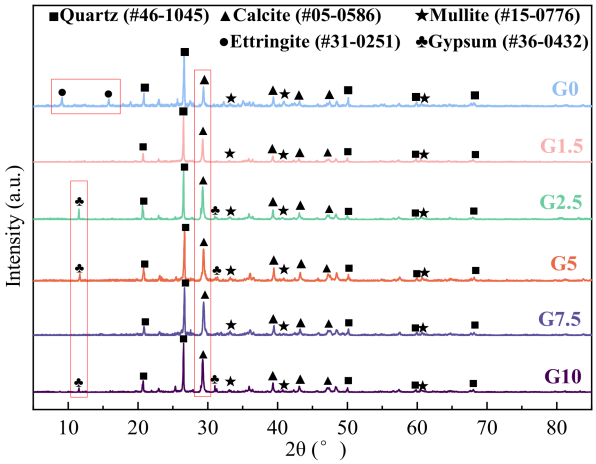


Figure 9. XRD patterns of CSCB under curing with different CO_2 concentrations.

Compared with the uncarbonated reference G0, the XRD patterns of the CO_2-cured samples (Figure 9) show the following changes:

The two characteristic peaks of ettringite (AFt, PDF #31-0251), 9.1° (100) and 15.8° (110), are clearly distinguishable only in the uncarbonated G0 sample and nearly disappear after CO_2 curing. This demonstrates that such aluminum-bearing hydration phases are decomposed and consumed during carbonation, which serves as direct evidence for "the difficulty in tracing aluminum-bearing minerals after carbonation". Only well-crystallized AFt can be directly identified by XRD in G0, while other aluminum-bearing phases (C-A-H, monosulfate phase, hydrogarnet, etc.) are inherently amorphous or of low crystallinity and overlap within the broad hump at 30–33°.

The (020) peak of gypsum ($CaSO_4 \cdot 2H_2O$, PDF #36-0432) at $2\theta \approx 11.6°$ is present only in G2.5, G5, and G10, but absent in G0, G1.5, and G7.5—i.e., its occurrence is non-monotonic with respect to the CO_2 concentration rather than simply "present after carbonation." This non-monotonic appearance may be attributed to two complementary factors. Primarily, gypsum precipitation is likely governed by the carbonation degree: at low CO_2 levels (G0, G1.5) sulfates remain incorporated in aluminate/hydrated phases, whereas at intermediate-to-high carbonation (G2.5, G5) they are released and recrystallize as gypsum; its absence in G7.5 may indicate further sulfate transformation under deeper carbonation. Additionally, because the 11.6° gypsum reflection is relatively weak and gypsum is sparsely distributed, sample micro-heterogeneity and the limited statistical representativeness of powder XRD cannot be excluded as contributors to its non-detection in G1.5 and G7.5. Carbonation nevertheless promotes the overall recrystallization of sulfates within the system or their precipitation as gypsum, which is associated with the decomposition of sulfur-aluminum-containing phases including AFt and the subsequent recombination of released SO_4^{2-}.

The calcite reflections increase systematically with the CO_2 concentration. The strongest calcite line, (104) at $2\theta \approx 29.4°$ (PDF 05-0586), grows in intensity. After normalizing each pattern to the quartz (101) internal standard, the relative intensity of the calcite (104) reflection rises from 38.6% in G0 to 50.5–70% in the carbonated samples (Table 4), confirming calcite as the dominant carbonation product and agreeing with the Ca–C enrichment observed by EDS and with the carbonate mass loss in the TG/DTG analysis (Section 3.1). The calcite peak width does not change appreciably, indicating that the crystal structure of the precipitated calcite is essentially the same under the room-temperature, ambient-pressure carbonation conditions employed. In contrast, the normalized intensities of quartz (101, fixed at 100 as the internal standard) and mullite (40.8°) remain essentially constant across all CO_2 concentrations, confirming that both phases are inert and do not par-

ticipate in the carbonation reaction—consistent with their origin as unreacted raw-material minerals (Table 1, Figure 1).

Table 4. Normalized relative intensities of the calcite (104) reflection.

Sample	CO_2 Concentration	Normalized Relative Intensity	Increase vs. G0
G0	0%	38.6%	0
G1.5	1.5%	50.5%	+30.8%
G2.5	2.5%	66.7%	+72.8%
G5	5%	64.2%	+66.3%
G7.5	7.5%	70.0%	+81.3%
G10	10%	67.2%	+74.1%

The only clearly resolved crystalline Al-bearing phase is ettringite (AFt), identified by its (100) and (110) reflections at $2\theta \approx 9.1^\circ$ and 15.8° (PDF 31-0251). Both are prominent in uncarbonated G0 but attenuate or vanish after CO_2 curing, indicating that early-hydration AFt is consumed as carbonation proceeds. Tracking the remaining Al-bearing phases by XRD alone is difficult for two reasons: (a) most Al-containing hydrates (C-A-H, C-A-S-H, hydrocalumite) and the dominant C-S-H gel are poorly crystalline or amorphous, contributing only to the broad diffuse scattering near 30–33°, where they are overlapped by quartz, calcite, and mullite; (b) even crystalline Al phases such as hydrogarnet (~33°) have weak principal reflections masked by stronger neighboring peaks. Consequently, the post-carbonation fate of these phases is established by the convergence of XRD, SEM/EDS, and TG evidence, whereas AFt consumption is directly demonstrated by its well-separated 9.1° and 15.8° reflections.

The strategy adopted here—relying on XRD (ICDD PDF cards) for phase identification while restricting SEM to morphology and EDS to elemental distribution, and cross-validating via TG–DTG—follows the multi-technique principle advocated for carbonated cementitious materials [32–34].

3.4. Mineral Sequestration and Strength Reduction Mechanisms

The possible reaction mechanisms discussed below are not derived from a single technique. They are inferred from the convergence of several independent lines of evidence: the unconfined compressive strength (UCS) tests (Section 3.2), the TG–DTG carbonation analysis (Section 3.1), the XRD mineral-phase identification (Section 3.3.3), and the SEM–EDS elemental mapping (Section 3.3.1). Because SEM micrographs alone cannot unambiguously identify individual crystalline phases (Section 3.3.2), the mechanistic interpretation offered in this section is a reasonable, integrated speculation supported jointly by these complementary results, rather than a claim based on microscopic morphology alone.

3.4.1. CSCB Forming Mechanism

Cement and some solid wastes in the CSCB system undergo hydration reactions to produce much calcium hydroxide (CH) and calcium silicate hydrate (C-S-H) gel and promote particle nucleation. After forming an alkaline environment, they drive the polycondensation reaction of hydration products to produce C_m-S_n-H_x and C_m-A_n-H_x gels with a high degree of polymerization as well as Ettringite (AFt). These materials are attached to the surface of solid-waste aggregate particles, further growing and filling the basic skeleton and pores between aggregate particles. They finally form a dense network skeleton with a certain mechanical strength. The mechanism driving the formation of CSCB is shown in Figure 10.

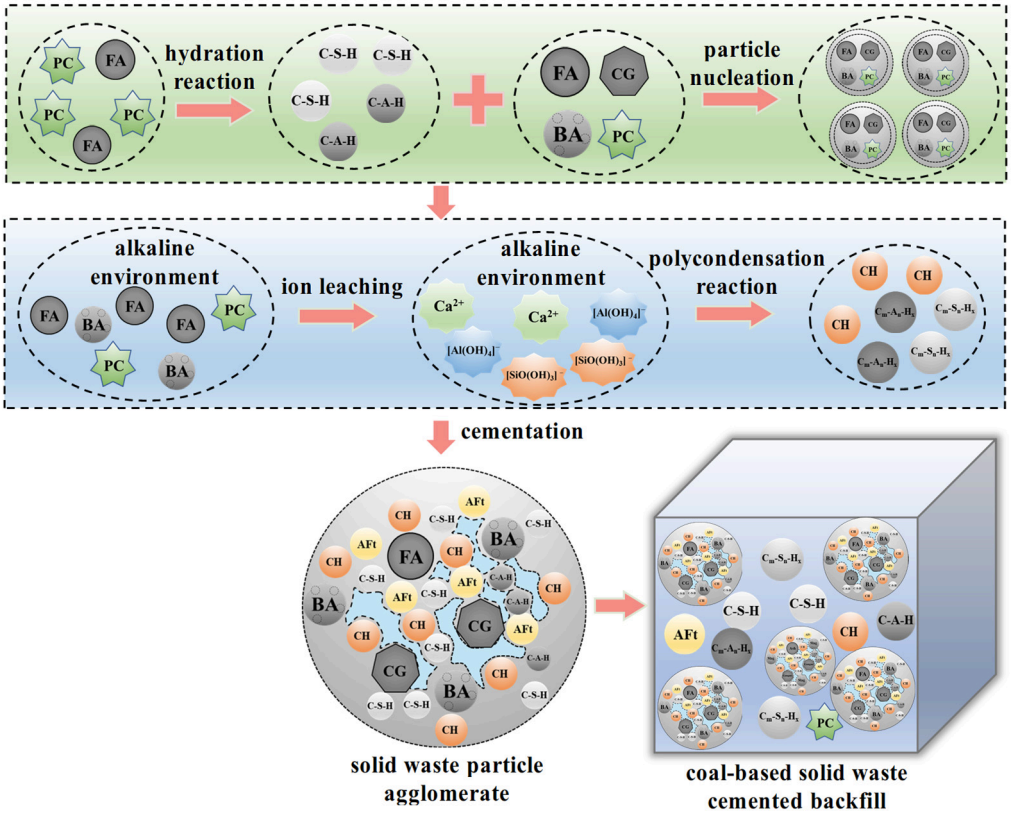


Figure 10. The formation of CSCB.

3.4.2. CO_2 Mineral Sequestration of CSCB

As outlined at the start of this section, the mineral sequestration mechanism of CSCB is inferred from the convergence of the UCS, TG–DTG, XRD, and SEM–EDS results. The CO_2 mineral sequestration process is the CO_2 adsorption process of calcium-bearing compounds in CSCB [CH, C-S-H gel, calcium aluminate hydrate (C-A-H) gel, and AFt], the principle of which is displayed in Figure 11.

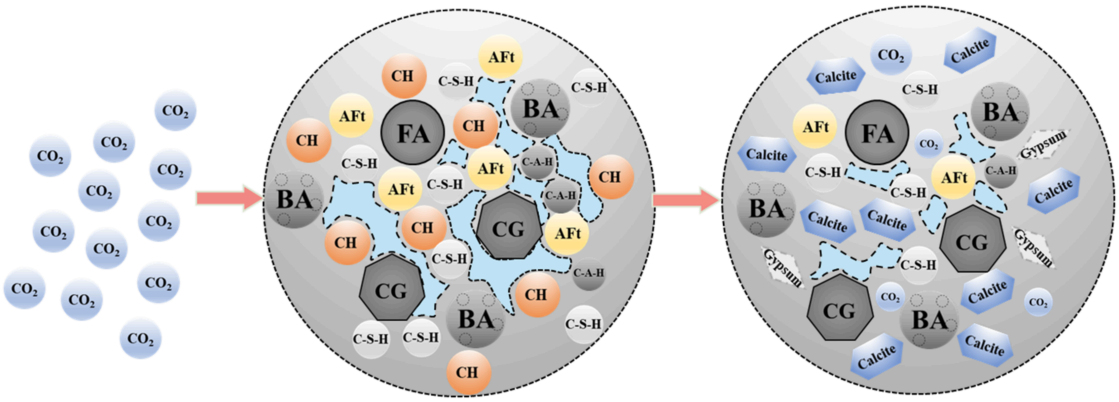


Figure 11. CO_2 mineral sequestration principle of CSCB.

The specific reactions are as follows:

CO_2 enters the backfill material via pores and is combined with water molecules to form H_2CO_3 which is unstable and easily ionized. Once H_2CO_3 is ionized, it releases H^+, HCO_3^-, and CO_3^{2-}, resulting in acidification of the interior of the backfill material and a decrease in the pH of the original alkaline environment. This pH decrease is a proposed

mechanism inferred from the mineralogical and microstructural evidence. The CaO present in FA reacts with water molecules to form $Ca(OH)_2$.

$$CO_2 + H_2O \rightarrow H_2CO_3 \quad (3)$$

$$CaO + H_2O \rightarrow Ca(OH)_2 \quad (4)$$

The solid wastes are hydrated to produce CH, which is combined with water molecules in the material in the later forming stage, thus changing from original colloids into hexagonal laminar crystals, which have hard surfaces and can adsorb other particles to form a whole. It can be expressed as follows:

$$H_2CO_3 + Ca(OH)_2 \rightarrow CaCO_3 + 2H_2O \quad (5)$$

After C-S-H and C-A-H gels adsorb CO_2, $CaCO_3$ precipitates are generated on the surface of mineral particle agglomerates. Although $CaCO_3$ exists as vaterite and aragonite, the structures of the two are unstable [35–37], so it is mainly present as calcite in the material. Therefore, it is calcite that has a relatively stable structure among mineralization products of CSCB, as expressed below:

$$\text{C-S-H}+CO_2 \rightarrow CaCO_3 + SiO_2(gel) + nH_2O \quad (6)$$

$$\text{C-A-H} + CO_2 \rightarrow CaCO_3 + Al_2O_3 \cdot H_2O \quad (7)$$

Ca-containing hydration products such as AFt further adsorb CO_2 and substitute some $CaSO_4$:

$$3CaO \cdot Al_2O_3 \cdot 3CaSO_4 \cdot 32H_2O + 3CO_2 \rightarrow 3CaCO_3 + 3CaSO_3 \cdot 2H_2O + 2Al(OH)_3 + 27H_2O \quad (8)$$

3.4.3. The Mechanism of Strength Reduction

Based on the above analysis of CO_2 mineral sequestration of CSCB, the mechanism underlying the strength reduction of CSCB was analyzed and attributed to three causes:

The alkaline environment is weakened or damaged (proposed mechanism). The strength of filling bodies is mainly ascribed to hydration products including the calcium silicate (alumino-) hydrate (C-(A)-S-H) gel and AFt produced by hydration of cement and some solid wastes, whereas the high CO_2 concentration is considered to weaken or damage the alkaline environment of the CSCB system—an inferred mechanism, as no direct pH or alkalinity measurement was performed—leading to insufficient hydration of cement and inhibiting the auxiliary gelation effects of solid wastes such as BA and FA.

The C-(A)-S-H gel is damaged. The newly generated C-(A)-S-H gel shows structural changes and is even decomposed under mineralization and carbonation reactions over time, thus substantially deteriorating the cementing performance of the filling body. The specific reactions are expressed by Equations (6) and (7).

AFt and CO_2 experience substitution reaction: AFt adsorbs CO_2 and undergoes the substitution reaction to produce new gypsum, as expressed by Equation (8). Previous research shows that the presence of an excessive amount of gypsum may interfere with the hydration reaction and exert adverse effects on the contraction in the hardening process, finally reducing the stability and durability of internal structure of the filling body [38,39].

In summary, although the newly generated calcite minerals to some extent fill the pores, the inferred damage to the alkaline environment and the decomposition and deterioration of the original gel structures by CO_2 appear to largely transcend the pore-filling effect. Finally, the strength of CSCB cured at a high CO_2 concentration is significantly reduced.

4. Conclusions

The evolution of the CO_2 uptake of CSCB under the influences of the CO_2 concentration was studied using the calculation method of the CO_2 uptake based on TG-DTG curves. As the CO_2 concentration rises from 1.5% to 10%, the CO_2 uptake of CSCB constantly increases by 86.90% from 2.52% to 4.71%. In the CO_2 concentration range of 0–10%, the relationship between the calculated CO_2 uptake of CSCB and the CO_2 concentration can be described by a Boltzmann fit. Because only five mineralized CO_2 concentrations were tested, this fit is presented as a descriptive representation of the observed trend within the investigated range rather than as a validated predictive model.

The evolution of the mechanical performance of CSCB under the applied curing and mineralization conditions was investigated. As the CO_2 concentration increases, the CO_2 uptake of CSCB increases while the strength reduces. The strength of CSCB cured without mineralization is 6.05 MPa, while that of CSCB mineralized at a 10% CO_2 concentration is only 0.72 MPa, reducing by 88.10%. The strength of CSCB is approximately linearly correlated with the CO_2 concentration.

The mechanism by which CSCB realizes CO_2 mineral sequestration was investigated and interpreted based on the combined experimental evidence. Changes in the chemical components and microstructures of CSCB after sequestrating mineral CO_2 were analyzed. In this way, the results suggest that CO_2 mineral sequestration of CSCB proceeds through the reaction of CO_2 with alkaline substances such as CH in CSCB and hydration products including C-(A)-S-H gel and AFt to produce carbonate mineralization products such as calcite.

The strength reduction mechanism of CSCB during CO_2 mineral sequestration was investigated and interpreted based on the combined experimental evidence. According to results and speculation, high CO_2 concentration may weaken the alkaline environment of the CSCB system leading to insufficient hydration of the cement, inhibiting the auxiliary gelation effects of BA and FA, and causing the degradation and decomposition of the C-(A)-S-H gel in mineralization and carbonation reactions. Meanwhile, the already-formed gel is inferred to undergo decalcification, and both of these phenomena are considered to contribute to the decrease in strength. Moreover, the results suggest that the hydration product AFt reacts with CO_2 through a substitution reaction to produce gypsum, which also contributes to the strength reduction of CSCB.

This study only examined the effect of CO_2 concentration under a single mix proportion and a 14-day curing age, and the generalizability of the conclusions requires further verification. It is recommended that future work include additional tests with varied mix proportions and extended curing ages (e.g., 28 days) to improve the understanding of the long-term performance of backfill subjected to carbonation. It should also be noted that this study is limited to laboratory-scale tests under idealized CO_2 distribution. The non-uniform CO_2 concentration caused by limited permeability in large-scale backfill bodies under field conditions has not been considered. Further validation via intermediate-scale trials or numerical simulations is therefore required. Moreover, parallel tests were not performed for the TG-DTG-calculated CO_2 uptake, and these data were not independently validated by alternative analytical methods such as elemental analysis or acid-base titration.

Author Contributions: Methodology, W.F. and B.H.; Writing—review & editing, W.F.; Formal analysis, D.Z.; Writing—original draft, D.Z.; Project administration, M.L.; Funding acquisition, M.L.; Conceptualization, M.L.; Supervision, B.H.; Investigation, Y.G. and Y.S.; Visualization, Z.L.; Data curation, Y.Z. All authors have read and agreed to the published version of the manuscript.

Funding: This research was funded by the National Natural Science Foundation of China, grant number 52274142.

Data Availability Statement: The data that support the findings of this study will be available from the corresponding author upon reasonable request.

Conflicts of Interest: The authors declare no conflicts of interest. The funders had no role in the design of the study; in the collection, analyses, or interpretation of data; in the writing of the manuscript; or in the decision to publish the results.

Abbreviations

The following abbreviations are used in this manuscript:

CSCB	Coal-based solid-waste cemented backfill
UCS	Uniaxial compressive strength
CG	Coal gangue
FA	Fly ash
BA	Bottom ash
PC	Portland cement
XRD	X-Ray diffraction
XRF	X-Ray fluorescence
SEM-EDS	Scanning electron microscopy-energy dispersive spectroscopy
TG	Thermogravimetric
DTG	Derivative thermogravimetric
C-S-H	Calcium silicate hydrate
C-A-H	Calcium aluminate hydrate
C-(A)-S-H	Calcium silicate (alumino-) hydrate
AFt	Ettringite
CH	Calcium hydroxide

References

1. Wang, S.; Lin, X.; Zhang, Y.; Wang, C. A Review of Utilizing Carbide Slag to Sequestrate Carbon Dioxide by Mineral Carbonation: Mechanisms, Processes, and Value-Added Products. *Fuel* **2025**, *384*, 134041. [CrossRef]
2. Delerce, S.; Benezeth, P.; Schott, J.; Oelkers, E.H. The Dissolution Rates of Naturally Altered Basalts at pH 3 and 120 °C: Implications for the in-Situ Mineralization of CO_2 Injected into the Subsurface. *Chem. Geol.* **2023**, *621*, 121353. [CrossRef]
3. Chen, S.; Li, Y.; Lin, J.-H.; Chang, C.-H. Energy Transition: Cap-and-Trade and Carbon Capture and Storage for Achieving Net-Zero Emissions with Sustainable Insurance. *J. Environ. Manag.* **2024**, *366*, 121902. [CrossRef] [PubMed]
4. Kinyar, A.; Bothongo, K. The Impact of Renewable Energy, Eco-Innovation, and GDP Growth on CO_2 Emissions: Pathways to the UK's Net Zero Target. *J. Environ. Manag.* **2024**, *368*, 122226. [CrossRef] [PubMed]
5. Cheng, H.; Wang, J.; Song, H.; Wang, B.; Ma, Z. CO_2 Mineralization Technologies Across Industrial and Geological Settings: Trends and Advances. *Min. Metall. Explor.* **2025**, *42*, 3271–3284. [CrossRef]
6. Suman; Rautaray, S.; Tripathy, A.; Das, D. CO_2 Sequestration Study on the Surface of Mechanically Activated Coal at Ambient Temperature and Pressure. *Energy Sources Part A-Recovery Util. Environ. Eff.* **2025**, *47*, 547–556. [CrossRef]
7. Jia, Q.; Shen, L.; Zhou, Z.; Wang, S.; Liu, L.; Wang, Y.; Li, Y.; Wang, J. Flowability, Carbon Sequestration, and Strength Properties of Carbonation-Cured Solid Waste-Based Backfilling Materials. *Energy Fuels* **2025**, *39*, 17990–18000. [CrossRef]
8. Ndlovu, P.; Chabalala, M.B.; Rampou, M.; Khumalo, S.P.-G.; Fashu, S.; Hungwe, D. Carbon Dioxide Utilization in Mineral Processing. *J. CO_2 Util.* **2025**, *94*, 103063. [CrossRef]
9. Zhang, X.; Liu, S.; Han, H. Analysis on Spatial Pattern Evolution and Policy of CO_2 Emissions from Economic Sectors in China from 2005 to 2020. *J. Environ. Manag.* **2025**, *394*, 127606. [CrossRef] [PubMed]
10. Tuzingila, R.M.; Kong, L.; Li, C.; Wang, Z.; Zanga Landu, C. Impact of Rock–ScCO_2 Interaction on Shale Features and Its Implication in CO_2 Geological Storage and Fracturing: Review and Perspectives. *Energy Fuels* **2025**, *39*, 18311–18349. [CrossRef]
11. Li, H.; Bian, Y.; Liu, M.; Lin, J.; Dai, M.; Xie, H.; Yu, H.; Chen, B.; Xue, M.; Li, Z.; et al. CO_2 Mineralization and Utilization by Tailings Sand in China for Potential Carbon Sinks and Spatial Project Layout. *Resour. Conserv. Recycl.* **2024**, *206*, 107598. [CrossRef]
12. Zhang, Y.; Ye, H.; Liu, Y.; Yang, Y.; Bai, L.; Zhang, L.; Li, J.; Wang, D. Compaction Layered Crushing Behavior and Acoustic Emission Response Characteristics of Gangue Solid Waste Backfill Material. *Appl. Sci.* **2026**, *16*, 2849. [CrossRef]
13. Fu, C.; Wang, C.; Zhang, F.; Chai, H.; Zhao, L.; Guan, X.; Zhu, J.; Zhang, H. Design and Properties of Paste Backfill Materials Based on Close Packing Theory. *Min. Metall. Explor.* **2025**, *42*, 2187–2203. [CrossRef]

14. Liu, H.; Deng, X.; Zheng, T.; Jia, N.; Zheng, Q.; Tian, X.; de Wit, B. Multi-Objective Ratio Optimization of Alkali-Activated Cemented Paste Backfill Mixtures Using the Sobol and Non-Dominated Sorting. *Min. Metall. Explor.* **2026**, *43*, 231–251. [CrossRef]
15. Xu, R.; Zhu, F.; Zou, L.; Wang, S.; Liu, Y.; Hou, J.; Li, C.; Song, K.; Kong, L.; Cui, L.; et al. CO_2 Mineralization by Typical Industrial Solid Wastes for Preparing Ultrafine $CaCO_3$: A Review. *Green Energy Environ.* **2024**, *9*, 1679–1697. [CrossRef]
16. Kumar, R.; Chung, W.J.; Khan, M.A.; Son, M.; Park, Y.-K.; Lee, S.S.; Jeon, B.-H. Breakthrough Innovations in Carbon Dioxide Mineralization for a Sustainable Future. *Rev. Environ. Sci. Bio-Technol.* **2024**, *23*, 739–799. [CrossRef]
17. Murugesu, M.P.; Joewondo, N.; Prasad, M. Carbon Storage Capacity of Shale Formations: Mineral Control on CO_2 Adsorption. *Int. J. Greenh. Gas Control* **2023**, *124*, 103833. [CrossRef]
18. Emmanuel, E.; Anggraini, V.; Syamsir, A.; Asadi, A. CO_2 Carbonation of Olivine-Admixed Marine Clay: Suitability for Bottom Liner Application. *Appl. Sci.* **2021**, *11*, 3164. [CrossRef]
19. Yi, G.; Tian, W.; Yuan, Q.; Cao, M.; Zhao, H.; Cheng, X. Revealing the Synergistic Mechanism of CO_2 Dosage and Granulated Blast Furnace Slag-Fly Ash Ratio on the Hydration-Mineralization Behavior of Cementitious. *Constr. Build. Mater.* **2025**, *494*, 143426. [CrossRef]
20. Zhao, Y.; Han, Y.; Xia, L.; Fang, Z.; Lu, D.; Jia, Q.; Gao, Y. Study on the Flow Properties of Modified Magnesium-Coal-Based Solid Waste Carbon Sequestration Backfill Materials. *Int. J. Greenh. Gas Control* **2025**, *146*, 104443. [CrossRef]
21. Li, B.; Long, K.; Cheng, W.; Fu, X.; Ma, J.; Zhang, S. Experimental Investigation into CO_2 Sequestration and Associated Ecological Behaviours of Carbon-Negative Backfilling with Coal Gangues. *Int. J. Greenh. Gas Control* **2025**, *147*, 104494. [CrossRef]
22. Cheng, Y.; Li, Z.; Li, J.; Gao, C.; Qin, C. Exploring the Enhancement on CO_2 Mineralization of Solid Wastes via Amine-Looping. *ACS Sustain. Chem. Eng.* **2025**, *13*, 3321–3330. [CrossRef]
23. Sun, W.; Liu, L.; Fang, Z.; Xie, G.; He, W.; Gao, Y. Experimental Study on the Production of Carbon-Absorbing Backfill Material from Freshly Mixed Modified Magnesium Slag Slurry. *Geomech. Geophys. Geo-Energy Geo-Resour.* **2024**, *10*, 10. [CrossRef]
24. Guo, Y.; Zhang, J.; Long, K.; Ma, J.; Gao, Y.; Li, B. Experimental Study on CO_2 Sequestration Capacity and Mechanical Characteristics Evolution of Solid Wastes Based Carbon-Negative Backfill Materials. *Constr. Build. Mater.* **2024**, *440*, 137457. [CrossRef]
25. Yan, B.; Hu, Y.; Huan, Q.; Liu, Z.; Lai, J.; Wang, S.; Song, M. Optimal Regulation of Modified Biochar in Solid Waste-Derived Lightweight Aggregates: Enhancing Carbonation Mechanisms and Negative Carbon Emissions. *Chem. Eng. J.* **2025**, *508*, 160920. [CrossRef]
26. Pan, Z.; Li, J.; Yue, X.; Wu, Z.; Zhang, D.; Hu, Y.; Ni, W.; Hitch, M. Temperature-Regulated Ammonium Carbonate Curing of Steel Slag: Enhanced Carbonation, Strength, and CO_2 Mineralization for Sustainable Building Materials. *J. Mater. Res. Technol.* **2025**, *38*, 893–904. [CrossRef]
27. He, W.; Liu, L.; Fang, Z.; Wei, B.; Jia, Q.; Zhu, M.; Wang, R.; Qu, H.; Gao, Y.; Xia, L. Effect of Long-Term Carbonation on Strength and Permeability of Magnesia-Coal Based Solid Waste Backfill Materials. *Process Saf. Environ. Prot.* **2025**, *194*, 892–903. [CrossRef]
28. Noh, S.; Triwigati, P.T.; Sim, G.; Lee, J.; Kim, E.; Moon, S.; Park, Y. Dual Benefits of Manganese Recovery and Carbon Mineralization via pH Swing-Assisted Carbonation Process in Iron and Steelmaking by-Products. *J. Environ. Chem. Eng.* **2025**, *13*, 115987. [CrossRef]
29. Wilcox, S.M.; Mulligan, C.N.; Neculita, C.M. Mineral Carbonation for Carbon Sequestration: A Case for MCP and MICP. *Int. J. Mol. Sci.* **2025**, *26*, 2230. [CrossRef] [PubMed]
30. Li, J.; Hou, Q.; Zhang, X.; Zhang, X. Microbial-Induced Mineral Carbonation: A Promising Approach for Improving Carbon Sequestration and Performance of Steel Slag for Its Engineering Utilization. *Dev. Built Environ.* **2025**, *21*, 100615. [CrossRef]
31. Qi, C.; Fourie, A. Cemented Paste Backfill for Mineral Tailings Management: Review and Future Perspectives. *Miner. Eng.* **2019**, *144*, 106025. [CrossRef]
32. Guleria, H.; Goyal, S. Investigating the Effect of Accelerated Carbonation Curing Duration on Portland and Pozzolana Cement-Based Concrete. *Struct. Concr.* **2026**, *27*, 4127–4146. [CrossRef]
33. Montes-Hernandez, G.; Perez-Lopez, R.; Renard, F.; Nieto, J.M.; Charlet, L. Mineral Sequestration of CO_2 by Aqueous Carbonation of Coal Combustion Fly-Ash. *J. Hazard. Mater.* **2009**, *161*, 1347–1354. [CrossRef] [PubMed]
34. Chen, B.; Miao, X.; Jia, B.; Wang, Y.; Hu, Z.; Peng, L. Total Recycling of Waste Concrete in Sustainable Concrete Production through CO_2 Mineralization: Strength, Durability, and Corrosion Issues. *Waste Manag.* **2026**, *214*, 115407. [CrossRef] [PubMed]
35. Li, J.; Yu, Q.; Huang, H.; Yin, S. Effects of Ca/Si Ratio, Aluminum and Magnesium on the Carbonation Behavior of Calcium Silicate Hydrate. *Materials* **2019**, *12*, 1268. [CrossRef] [PubMed]
36. Seifu, M.N.; Bersisa, A.; Moon, K.-Y.; Kim, G.M.; Cho, J.-S.; Park, S. Exploring Reaction and Carbonation Products of Calcium Silicate Cement. *J. CO_2 Util.* **2023**, *71*, 102471. [CrossRef]
37. Hashim, M.S.; Kaczmarek, S.E. The Transformation of Aragonite to Calcite in the Presence of Magnesium: Implications for Marine Diagenesis. *Earth Planet. Sci. Lett.* **2021**, *574*, 117166. [CrossRef]

38. Chiloane, N.M.; Mulenga, F.K. Revisiting Factors Contributing to the Strength of Cemented Backfill Support System: A Review. *J. Rock Mech. Geotech. Eng.* **2023**, *15*, 1615–1624. [CrossRef]
39. Tang, Y.; Zheng, J.; Guo, L.; Zhao, Y. Effect of Gypsum Addition on the Mechanical and Microstructural Performance of Sulphide-Rich Cemented Paste Backfill. *Minerals* **2021**, *11*, 283. [CrossRef]

Disclaimer/Publisher's Note: The statements, opinions and data contained in all publications are solely those of the individual author(s) and contributor(s) and not of MDPI and/or the editor(s). MDPI and/or the editor(s) disclaim responsibility for any injury to people or property resulting from any ideas, methods, instructions or products referred to in the content.